Article

SUAS Based Multispectral Imagery for Monitoring Wetland Inundation and Vegetation

Dustin Dehm [1], Richard Becker[1,2], and Alexandra Godre[1]

[1] University of Toledo, Department of Environmental Sciences, Toledo, OH 43606 USA
[2] University of Toledo, Lake Erie Center, Toledo, OH 43606 USA
* Correspondence: Richard.Becker@utoledo.edu; Tel.: (419)-530-4571

Abstract: Mapping short-term wetland vegetation and water storage changes is valuable for monitoring the biogeochemical processes of wetland systems. Old Woman Creek National Estuarine Research Reserve is a dynamic freshwater estuary that experiences intermittent changes in water level over the course of a year. Small unmanned aerial systems (sUAS) are useful tools in monitoring changes as they are rapidly deployed, repeatable, and high-resolution. In this study, commercial quadcopters were paired with a red/green/near-infrared MAPIR Survey 3W camera to produce normalized difference vegetation index (NDVI) and normalized difference water index (NDWI) maps to observe short-term changes at OWC. Orthomosaics were produced for flights on 8 days throughout 2018 and early 2019. The orthomosaics were calibrated to bottom-of-atmosphere reflectance using the Empirical Line Correction method and NDVI and NDWI maps were created. The NDVI pixel values were used to generate maps of vegetation extent showing density changes over time. Identifying dominant vegetation in these maps allowed for the application of the National Estuarine Reserve System (NERRS) Classification Codes to zones of interest. NDWI provided water extent at different water levels and when paired with LiDAR and bathymetric data yielded water volume and residence time estimates. The produced maps contribute to the overall understanding of habitats affected by water inundation variations.

Keywords: sUAS; UAV; drone; multispectral; wetland; NDVI; NDWI; remote sensing; NERRS

1. Introduction

Wetland systems serve as valuable water resources that filter water from upland areas, are a habitat for many species of plants and animals, and serve as a recreational nature area for the community [1-4]. Currently, wetland monitoring methods by remote sensing are mainly satellite and fixed-wing manned aircraft-based platforms. Satellite systems such as the European Space Agency's [5] Sentinel-2 offer frequent revisits every 2-5 days at a 10-meter pixel resolution [6], while fixed-wing manned aircraft such as the National Agriculture Imagery Program (NAIP) have higher resolution (1-meter) than satellite imagery [7], but are only flown every 2-3 years due to the costs of flights. Wetlands are also monitored at ground level via line-of-sight observations or point measurements by foot or by boat.

Old Woman Creek (OWC) (Figure 1a) was selected as the study site for this method because it experiences rapid changes in water level due to the seasonal or sudden closure and opening of a barrier beach where it connects to Lake Erie [2, 8]. It is also the only freshwater National Estuarine Research Reserve on Lake Erie [2]. OWC is the outlet for about 70 km² of mostly agricultural land and is a nutrient sink for agricultural runoff [9]. The defining characteristic of OWC is the barrier beach on the northern side of the estuary connecting the wetland to Lake Erie and classifies the wetland as a barred drowned river-mouth (Figure 1b) [10]. The barrier beach is seasonally breached in early winter and again in spring when water storage builds up and overtops the beach, resulting in a dramatic drop in water level [2]. The beach can also be breached short term events such as

46 upstream precipitation, changes in the level of Lake Erie, or strong storm events [2, 11]. The beach
47 has also been breached unnaturally by the local community when high water levels were overtopping
48 and threatening the integrity of privately owned rip-rap on a side channel to the east. This sudden
49 opening of the beach resulted in about a one-meter drop in water level over a 24-hour period,
50 drastically changing the habitats in the main basin. The wetland's deepest point is the main channel
51 as it passes under the Route 6 bridge to the north and can be as deep as 3.6 meters, but most of the
52 main basin is sub-meter in depth [11].
53

(a)   (b)
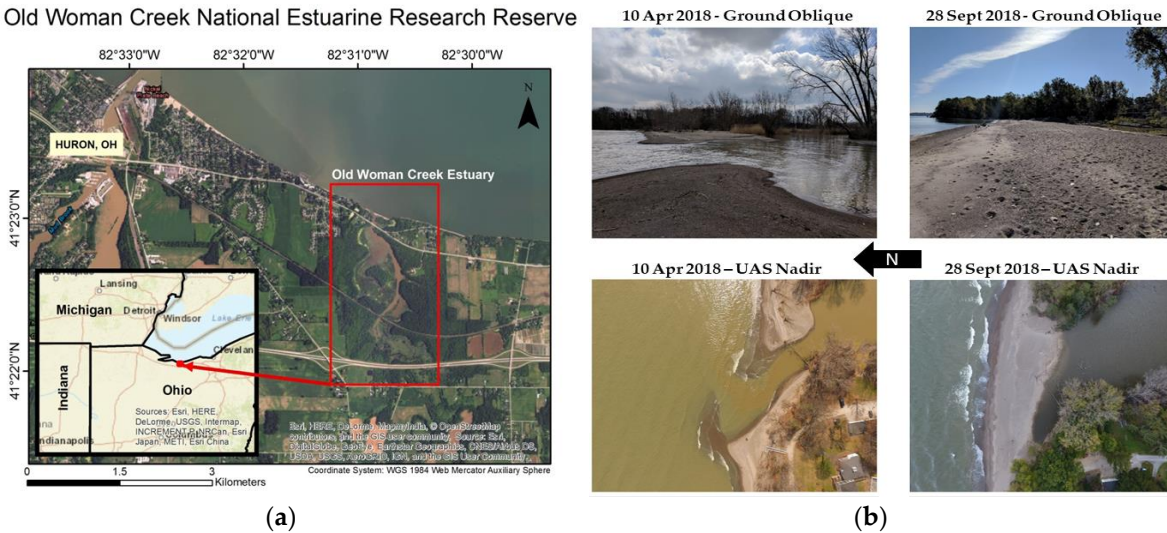
54 **Figure 1.** (**a**) Study Site; (**b**) Open and closed examples of barrier beach on the north side of OWC

55 These rapid changes are not captured well using current remote sensing methods. Satellite
56 imagery does not do well at defining smaller areas of inundation and distinguishing the shoreline
57 due to pixel mixing and revisit scenes that are often rendered ineffective by cloud cover [12]. Fixed-
58 wing manned aircraft imagery is not acquired frequently enough here to capture any seasonal change
59 but can be useful as a snapshot of long-term habitat changes. SUAS offer a higher temporal and
60 spatial resolution solution with flexible and more controlled revisit times [13, 14].
61 Unmanned aircraft have been used to observe the Earth's surface since at least the mid-19th
62 century [13]. In the recent past sUAS use was hindered by the need for custom or expensive platforms,
63 weight limitations for more specialized equipment, and changing governmental regulations on
64 unmanned aerial flight [15]. Recent advances in the miniaturization of remote sensing hyperspectral
65 and multispectral sensors and advances in cost-effective commercial unmanned aerial vehicles
66 (UAV) platforms have made environmental research much more accessible using these systems [16,
67 17]. Modern use of UAV's in environmental monitoring have included observing rangelands [18],
68 ecohydrology applications [19], coastline identification [20], and vegetation monitoring [21], to name
69 a few.
70 The focus of this study is the effectiveness of lightweight low-cost sUAS based multispectral
71 cameras in mapping short-term wetland emergent vegetation and water inundation changes over
72 time [22]. Models produced via remote sensing methods have suggested global wetland areas will
73 continue to decrease due to increased drought and climate change [23]. These predictions
74 substantiate the need for monitoring wetland habitats in the short and long term. Although this
75 project was designed for OWC, the methods described here could be applied to any environmental
76 situation where water inundation and vegetation required monitoring. Applications of this method
77 could include restored or engineered wetlands, flood monitoring, river channel migration, invasive
78 species monitoring, etc. as it pertains to monitoring vegetation and water inundation changes.

79 **2. Materials and Methods**

80   This study used two commercial Dà-Jiāng Innovations [24] (https://www.dji.com) Phantom
81   UAV as flight platforms. The Phantom 3 Professional and the Phantom 4 Standard quadcopter
82   models were affordable and provided flexibility in takeoff and landing sites. The payload capacity
83   of both UAVs was enough to carry the 76g MAPIR Survey 3W camera with approximately 25
84   minutes of flight time. The MAPIR Survey 3W (https://www.mapir.camera) Red/Green/Near-
85   Infrared (RGN) Sony Exmor R IMX117 12 MegaPixel (MP) camera employs a complementary
86   metal-oxide semiconductor (CMOS) chip and has bands at 660 nanometers (nm), 550 nm, and 850
87   nm. The CMOS sensor exposes a line of pixels at a time to detect photons, and transfers the
88   information while the next line is exposed [25]. The CMOS sensor is cheaper and uses lower battery
89   power than the traditional charged-couple device (CCD) array, and recent advances in CMOS
90   technology makes them ideal for affordable sUAS applications [25]. The Phantom 3 and Phantom 4
91   are also equipped with a 12.4 MP red/green/blue (RGB) camera.

92   All flights were conducted in accordance with the Federal Aviation Administration (FAA) Part
93   107 regulations by licensed remote pilots [26]. Visual observers were also used to confirm and
94   report the position of the UAV during flights. Flights were scheduled between 9AM and 11AM at
95   OWC to avoid excessive pedestrian traffic in the reserve and to keep incident sun angles consistent
96   throughout scenes. Flights were programmed and flown using the automated flight software
97   DroneDeploy (https://www.dronedeploy.com/). Flights were set up with 65-70% side and 75% front
98   overlap between RGB images at 120-meter altitude above ground level [27] with flight speeds of
99   approximately 14-meters per second. The cameras on the UAV were positioned pointed nadir for
100   all flights. The Survey 3W RGN camera was set to acquire images at either 1.5 seconds per photo for
101   JPG files or 2.75 seconds per photo for RAW+JPG acquisition [28] via its built-in timer software and
102   had greater side and front overlap than the Phantom RGB photos. Flights were conducted in spring,
103   fall and winter (Table 1). Summer flights were not conducted because of increased visitor traffic
104   during flight hours and increased manned aircraft activity in the area of the study site during these
105   months.

106   **Table 1.** Flight data

Date	Atmospheric Conditions	Time Flown	Vegetation Conditions	Initial Images Acquired
10-Apr-18	Mostly Cloudy	10AM-12PM	Leaf-Off	397
23-Apr-18	Sunny	9AM-11AM	Leaf-Off	1747
17-May-18	Sunny	9AM-12PM	Leaf-On	1681
29-May-18	Sunny	9AM-11AM	Leaf-On	448
28-Sep-18	Sunny	9AM-11AM	Mid-Abcission	1948
24-Oct-18	Mostly Cloudy	10AM-11AM	Mid-Abcission	735
25-Oct-18	Sunny / Hazy	9AM-11AM	Mid-Abcission	1631
30-Oct-18	Mostly Cloudy	9AM-11AM	Mid-Abcission	878
14-Nov-18	Mostly Cloudy	9AM-11AM	Late-Abcission	642
22-Feb-19	Fair	8AM-11AM	Leaf-Off	1349

107

108   Five ground control points (GCP) were used to increase the orthomosaic's vertical and
109   horizontal accuracy. White and black high contrast plywood boards measuring 60 x 60-centimeters
110   were placed upon three National Geodetic Survey (NGS) benchmarks located in the study area that
111   could be easily seen in images [29]. One additional GCP was created via a laser level survey using
112   one of the NGS benchmarks as a base station. Another artificial GCP was created by identifying a
113   feature in both a LiDAR digital elevation map (DEM) and imagery and setting a higher level of

114 error [30]. For calibration purposes, a Spectralon board of 99% reflectance was set out before each
115 flight. The Spectralon board and other homogeneous and spectrally stable surfaces were measured
116 with an ASD FieldSpec Pro spectrometer several times throughout the study as calibration and
117 validation targets [31, 32]. ASD measurements were acquired using an 8-degree foreoptic. White
118 references were taken 10 times from approximately a meter above a 99% reflectance Spectralon
119 board [33]. The ratio of upwelling to downwelling irradiance results in a reflectance value. The
120 surfaces used to calibrate scenes were selected because of their spatial and spectral stability over
121 time so they could be used across multiple scenes [31, 32]. Examples of calibration surfaces include
122 the Spectralon board, roads, sand, parking lots, the drone carrying case, and the university truck.

123   Agisoft Photoscan (https://www.agisoft.com) structure from motion (SfM) software was used
124 to create the orthomosaics from flight images [34]. The SfM software identifies common tie points
125 between image overlap and uses each image's geo-location and UAV orientation to stitch images
126 together without geometric distortion as an orthomosaic [35, 36]. A modified SfM workflow from
127 the U.S. Geological Survey (USGS) National Unmanned Aircraft Systems Project Office was used to
128 process the flight imagery [37] (Figure 2).

Agisoft Photoscan Workflow
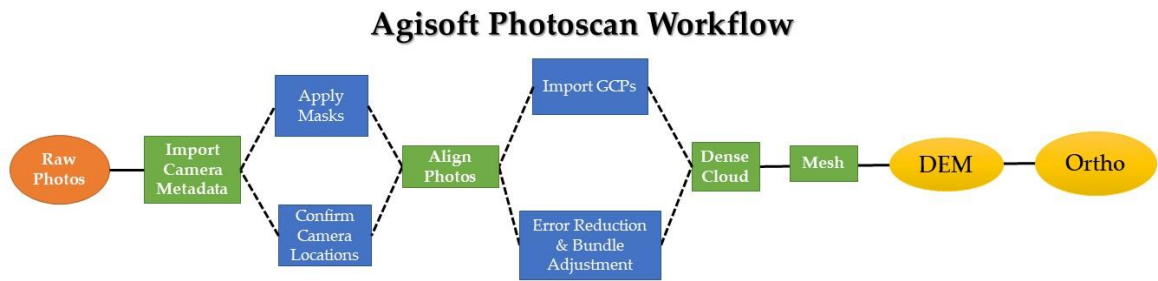
129   **Figure 2.** Agisoft Photoscan workflow

130   After images were imported into Agisoft Photoscan masks were applied to areas of sun-glint,
131 saturation, and distortion. The photos were then aligned using key points and tie points defined as
132 significant features identified in multiple images [34, 38]. Aligned points create a sparse cloud of
133 points and the GCPs were imported to refine the alignment. An error reduction and bundle
134 adjustment was run to eliminate tie points with low accuracy [39]. Once only high confidence tie
135 points remained, a dense point cloud was created from the other pixels in each image and a mesh
136 was created. A dense point cloud is a grouping of points with known X, Y, and Z coordinates [38].
137 Agisoft then creates a triangulated irregular network (TIN) mesh from the point cloud using the
138 Delaunay triangulation method [38, 40]. From the mesh, a DEM and orthomosaic were created and
139 exported for calibration.

140   The uncalibrated orthomosaics were imported into Environment for Visualizing Images
141 (ENVI) (Exelis Visual Information Solutions, Boulder, Colorado) software for calibration of digital
142 numbers (DN) to bottom-of-atmosphere reflectance using the empirical line correction (ELM)
143 method [41, 42] . The DNs were calibrated to reflectance using surfaces of known spectral
144 properties within the scene that were measured using the ASD FieldSpec Pro spectrometer.
145 Reflectance values calculated from both a bright and dark target were applied to the images. In any
146 given mosaic, two to five surfaces were used as calibration targets, while two to four surfaces were
147 reserved as validation targets. Calibration also included geospatial corrections from errors in the
148 orthomosaic process and camera locations. Scenes were georeferenced in relation to each other to
149 ensure habitat extent changes were accurate.

150   The calibrated scenes were used to calculate spectral indices. NDVI is the ratio of red light
151 absorbed by plants for use in photosynthesis to the amount of near-infrared reflected by the cellular
152 wall structure of healthy plants, and was developed to exploit the spectral properties of vegetation

[25, 43]. NDVI values were between -1 and 1 and were classified in different ranges to identify vegetation in 6 NDVI maps. These maps captured the changes in vegetation coverage over the time period of the study and were quantified as percentages above a 0.2 threshold. Vegetation changes were summarized for emergent vegetation. Values closer to 1 represent more dense and healthy vegetation and values below 0 represent non-vegetation surfaces such as water, concrete, sand, etc. NDVI values were classified as vegetation and non-vegetation. Classifications followed the USGS classification scheme of NDVI where values below 0.2 are no vegetation, 0.2-0.5 is sparse vegetation or unhealthy vegetation, and 0.6-0.9 is dense or healthy vegetation [44]. A pixel was considered vegetation in the orthomosaics if NDVI exceeded 0.2. Extents were calculated for an area of interest at OWC across scenes from different times of the year to calculate emergent vegetation changes. Various dominant emergent vegetation types were identified using their visual and spectral properties and were segmented into polygons manually. To validate the identified vegetation types, volunteers and OWC staff conducting wildlife habitat surveys provided their data from similar time periods within days of the flight surveys to identify dominant species in each polygon. An area of dominant vegetation was then quantified by extent polygons over spectrally and texturally similar areas validated by the ground vegetation surveys. The NERRS classification schemes used to classify and quantify wetland habitat were then applied to the dominant plant species and extent in Zone 1; an area of interest to ecologists working at OWC [22, 45]. The method described here classified each polygon to the subclass level and additional information down to the dominant species of each polygon. Zonal statistics were used to calculate emergent vegetation extent at Zone 1.

NDWI is the ratio of green light reflected to near-infrared absorbed by water. Water absorbs light in the green band of the Survey 3W but tends to absorb much more in the near-infrared, and the ratio between absorption in the green and NIR allows for the delineation of water **features [46].** Like NDVI, NDWI values are between 1 and -1 , with values above 0 representing water features and values below 0 representing non-water surfaces. NDWI maps were created to calculate the extent of open water during various conditions across multiple scenes using these water and non-water surfaces. NDWI paired with bathymetric data also allowed for estimates of water volume in the main basin, and when paired with upstream USGS stream discharge data [47] provided estimates of residence time using the available bathymetric data. NDWI values were classified into water and non-water features, visualized to show inundated areas in each scene and were combined with available ancillary data to further utilize the NDWI maps. Data available for OWC included a current bathymetric survey and USGS discharge. Though NDVI can be used as a mask for water extent, NDWI was chosen due to its slightly higher performance for open water identification [48, 49].

Because water surface elevation cannot be calculated accurately using photogrammetric methods due to the specular nature of the water, and constantly changing angles of the waters surfaces due to water motion, shoreline water levels were found using NDWI values and a combined bathymetric and LiDAR dataset. A transect was drawn across the main basin and higher confidence open water pixels are only concentrated at or below the shoreline elevation (Figure 3). This method allowed for shoreline classifications to be calculated for scenes with leaf-off conditions. The shoreline values were validated using a YSI WaterLOG Nile 502 Radar sensor (https://www.ysi.com/Nile) mounted on the bridge at Route 6 and a weather station at Marblehead, OH (41° 32.6' N, 82° 43.9' W) operated by the National Oceanic and Atmospheric Administration (NOAA) [29, 50]. Water volume for the main basin was calculated using the "Surface Volume" toolbox feature in ArcGIS. The shoreline value found was used as a baseline elevation and a volume was calculated using all pixels with an elevation below it. These volumetric calculations were also compared to previous calculations done by Herdendorf et al. in 1990 [11] [2].
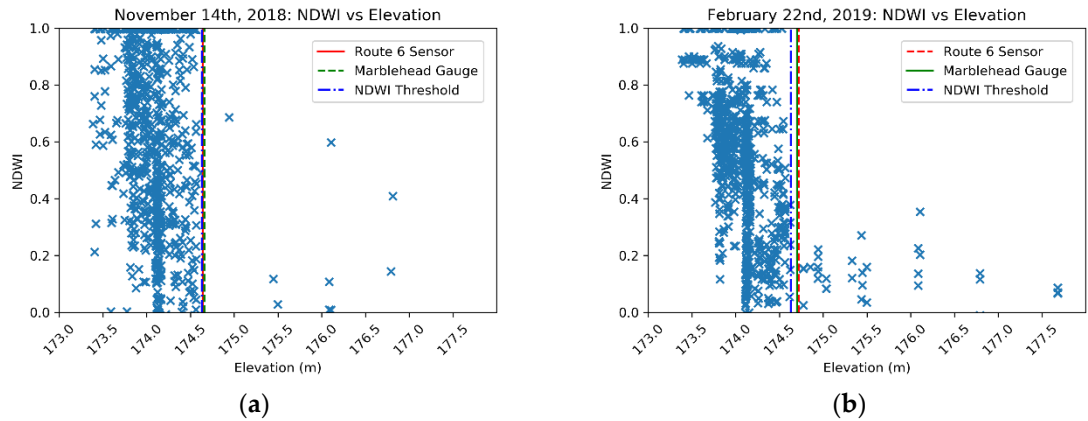
Figure 3. Open water pixels (blue) at different elevations across the transect for November 14th, 2018 (**a**) & February 22nd, 2019 (**b**) compared to water elevation readings from the microwave sensor (red) on the Route 6 bridge and the gauge at Marblehead (green).

Residence time for the flowing part of the main basin was also calculated. The flowing part of the basin was identified using turbidity differences. Turbidity increases with sediment transport and shifts wavelength peaks towards the green [25]. The area of flow volume (V) combined with discharge (Q) values from the USGS streamflow gauge (04199155) [47] upstream from OWC allowed for residence time (Tr) to be calculated using:

$$Tr = V / Q$$

3. Results

3.1. Flights & Orthomosaics

A total of 10 flights were conducted throughout early 2018 to early 2019 [26] (Table 1). Flight times for a single flight averaged between 10-15 minutes for larger areas at about 12 m/s. Overlap coverage was sufficient both for the Phantom based cameras and the Survey 3W. The Survey 3W was flown using both JPEG and RAW file formats. RAW format pictures take longer for the camera to process and store, and storage space was limited to about 3-4 flights. RAW format pictures did overlap enough for othomosaics and produced high quality orthomosaics, but the higher frequency of JPEG images allowed for more quality control on images that may have experienced significant sunglint or blurring at the cost of data loss due to compression [51].

Overlap for both cameras and file formats was sufficient to create the orthomosaics. A total of 16 orthomosaics were created in Agisoft Photoscan, 8 from the RGN Survey 3W and 8 from the RGB Phantom cameras [22]. The RGN orthomosaics acquired data with no problems on all flights, and the image overlap was sufficient to create orthomosaics of the study areas of intersest. The RGB camera had acquisition issues on some flights, where the automatic image acquisition was not activated at the start of the flight route. This led to areas of data loss in some scenes. However, analysis was still possible using only the RGN cameras. Other environment issues included variable cloud cover and sunglint (Figure 4). Variable cloud cover led to repeating cloud images on reflective surfaces, namely water. Sunglint resulted in saturation in pixels that had to be masked from images. The high overlap of imagery meant masking some of the more distorting features did not seriously affect the photogrammetric process in most cases.

(**a**)   (**b**)
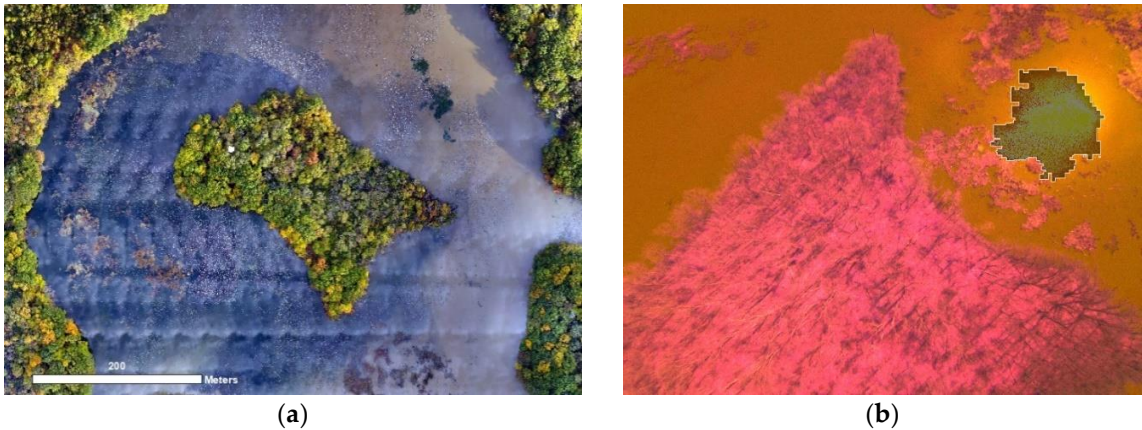
Figure 4. (**a**) Variable cloud cover conditions result in a repeating cloud reflection pattern in orthomosaic; (**b**) Example of sun-glint and applied mask in an RGN photo.

3.2 Calibration

The heterogeneous and temporally stable targets used to calibrate the orthomosaics proved sufficient to attain bottom-of-atmosphere reflectances even though the scenes and ASD spectrometer measurements were often temporally different. The root-mean squared and mean absolute error of each orthomosaic scene were calculated to obtain how well each scene calibrated relative to the ASD measurements (Table 2). The RMSE and MAE values reperesent how well the observed surface values used for calibration and validation match the ASD and not necessarily the actual reflectance on the ground.

Table 2. RMSE and MAE for each orthomosiac.

Date	RMSE Calibration	RMSE Validation	RMSE Combined	MAE Calibration	MAE Validation	MAE Combined
23-Apr-18	0.051	0.038	0.044	0.042	0.030	0.035
17-May-18	0.078	0.095	0.086	0.054	0.074	0.063
28-Sep-18	0.074	0.096	0.076	0.059	0.076	0.059
25-Oct-18	0.053	0.034	0.045	0.033	0.026	0.030
30-Oct-18	0.089	0.061	0.081	0.070	0.050	0.064
14-Nov-18	0.050	0.078	0.068	0.038	0.071	0.049
22-Feb-19	0.083	0.029	0.068	0.063	0.022	0.049

3.3 NDVI

NDVI maps allowed dense or healthy vegetaiton to be distinguished easily (Figure 5). The spatial resolution of the RGN maps allowed for shape and texture of individual plants or plant species to be used concurrently with NDVI for classification purposes. Emergent vegetation short term changes and seasonal variability could be observed quickly throughout the timeline of maps (Table 3).
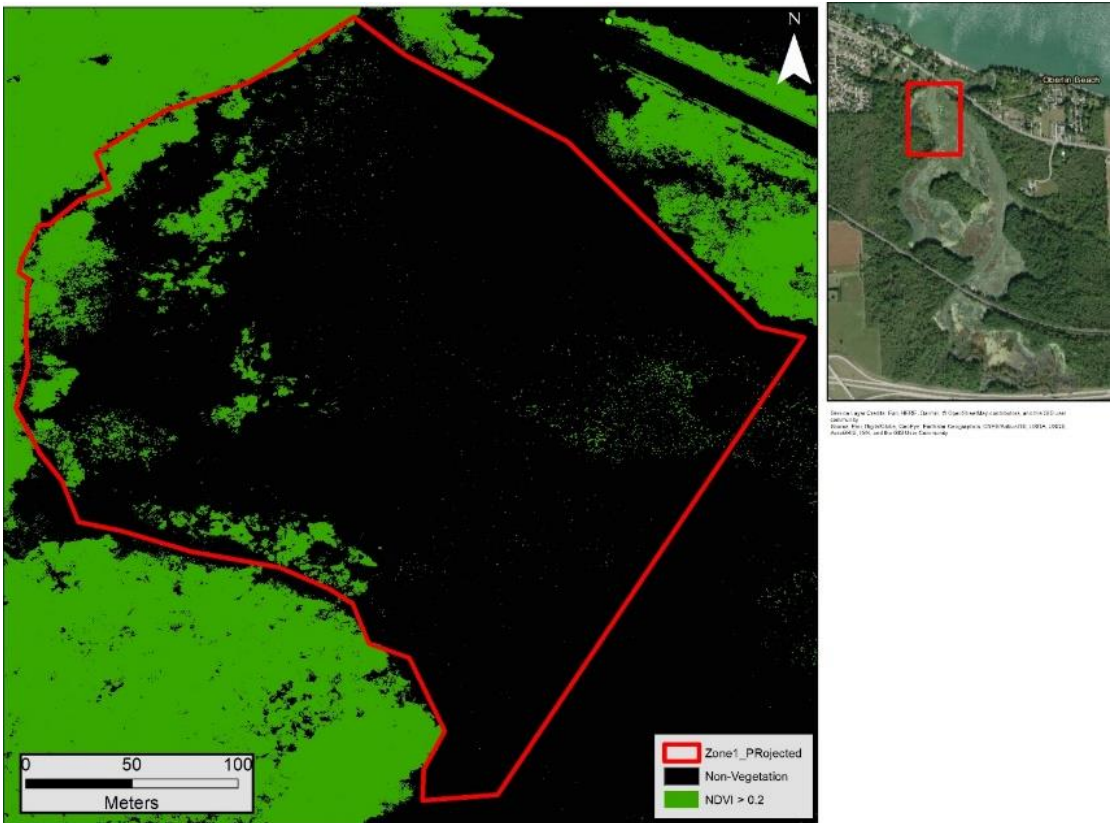
Figure 5. NDVI Zone 1 Analysis on October 25th, 2018.

During dense leaf-on conditions there was some saturation in NDVI values. Differences in specific values in NDVI are probably not significantly different after a certain density of vegetation, such as the difference between 0.5 and 0.7 in a scene [52]. There were also problems in some scenes where both the visible and NIR bands were saturated because the orientation of the sun and the sensor resulting in low NDVI values.

Table 3. Emergent Vegetation NDVI Results at Zone 1.

Zone 1 NDVI Statistics								
Date	Pixels NDVI > 0.2	Pixel Size (m)	Pixel Area (m^2)	Vegetation Area (m^2)	Zone 1 Polygon (m^2)	Vegetation %	Mean NDVI	Std Dev
23-Apr-18	921,065	0.051	0.0026	2,394	56,444	4.2	-0.67	0.38
28-Sep-18	16,187,148	0.050	0.0025	40,477	56,444	71.7	0.30	0.15
25-Oct-18	2,178,968	0.046	0.0021	4,630	56,444	8.2	-0.69	0.46
30-Oct-18	3,085,460	0.045	0.0020	6,276	56,444	11.1	-0.35	0.45
14-Nov-18	530,100	0.051	0.0026	1,370	56,444	2.4	-0.47	0.36
22-Feb-19	198,569	0.048	0.0023	458	56,444	0.8	-0.35	0.21
**Note: 17 May displayed significant shift of the red band which did not pass QC checks.								

3.4 NDWI

NDWI maps showed areas of water inundation well (Figure 6). When combined with the validated shoreline data, the inundation maps provided a complete picture of which areas were inundated at what water levels. Shoreline water elevations were only created during leaf-off conditions, as during leaf-on conditions the sensor could not detect the water-land boundary.
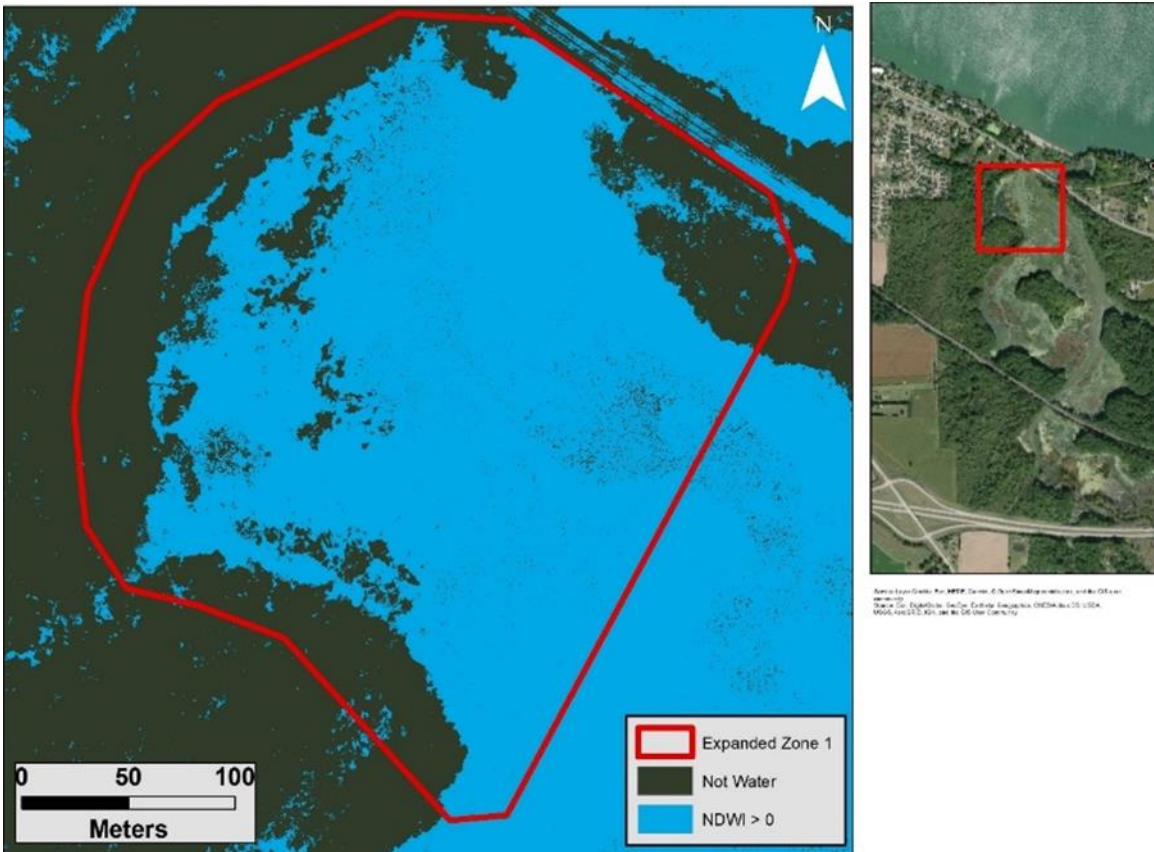
Figure 6. NDWI map at Zone 1 on October 25th, 2018.

The 7 NDWI maps (Table 4) produced comprehensive estimates of open water area and provide a comprehensive picture of water inundation, especially in leaf-off and low vegetation conditions. Calculated shorelines generally agreed with the readings from the Route 6 bridge and the NOAA Marblehead water gauge approximately 25 km northwest of OWC for the three days of leaf-off conditions. During all of these leaf-off days, the beach was open and OWC was hydrologically connected to Lake Erie. Shoreline calculations worked best in areas free of floating debris and overhanging or fallen trees with land-to-water transitions of lower elevation change slopes. The presence of steep bluffs on much of the shoreline make finding gentle slopes visible to the sUAS difficult in the main basin. Pixel sizes for the sUAS imagery ranged from 4.5 to 5.1 centimeters per side.

Table 4. NDWI map results from Zone 1.

Date	Open Water Pixels	Open Water Area (m^2)	Open Water (%)	Bridge Water Elevation (m)	sUAS Water Elevation (m)	Lake Erie Water Level (m)	Leaf Condtion
23-Apr-18	21,677,518	56,349	68.05	174.98	174.85	174.92	Off
17-May-18	19,447,758	48,622	58.72	174.98	NA	174.96	On
28-Sep-18	11,950,639	29,883	36.09	175.58	NA	174.61	On
25-Oct-18	26,652,148	56,627	68.38	175.43	NA	174.56	On
30-Oct-18	25,602,420	52,075	62.89	175.72	NA	174.63	On
14-Nov-18	22,059,928	57,032	68.87	174.64	174.63	174.66	Off
22-Feb-19	25,688,115	59,297	71.61	174.72	174.63	174.70	Off

When comparing the volumetric and residence time calculations (Table 5) from the sUAS and those done by Herdendorf et al. in 1990, the newer bathymetric survey should be a more accurate measure of the present day depths along the basin, although it was incomplete at the time of this publication. The bathymetric survey used for this study does not cover approximately 56,133

279 m² (13.9 acres) of the southwestern side of Star Island. Differences may also be the result of changes
280 to the bottom of the estuary between 1990 and 2019.

281 **Table 5.** Volume & Residence Time Comparisons.

Date	sUAS Water Elevation (NAVD 88)	sUAS Volume: Main Basin (m³)	USGS Discharge (m³/s)	sUAS Residence Time: Main Basin (days)	Channel Volume (m³)	Channel Residence Time (Days)	1990 Survey Water Volume (m³)	Basin % Difference (1990 vs sUAS)
23-Apr-18	174.85	318,168	0.317	12	144,295	5	350,000	9.1
14-Nov-18	174.63	231,121	0.595	4	110,772	2	245,000	5.7
22-Feb-19	174.63	231,121	1.17	2	110,772	1	245,000	5.7

283 *3.5 Classification & Analysis*

284 A manual classification was used to identify vegetation habitats and species. NDVI was used
285 to identify spectral differences and stages of senescence in plant species, and the high-resolution of
286 the datasets allowed for texture and spatial shapes (Figure 7a) to be used to separate dominant
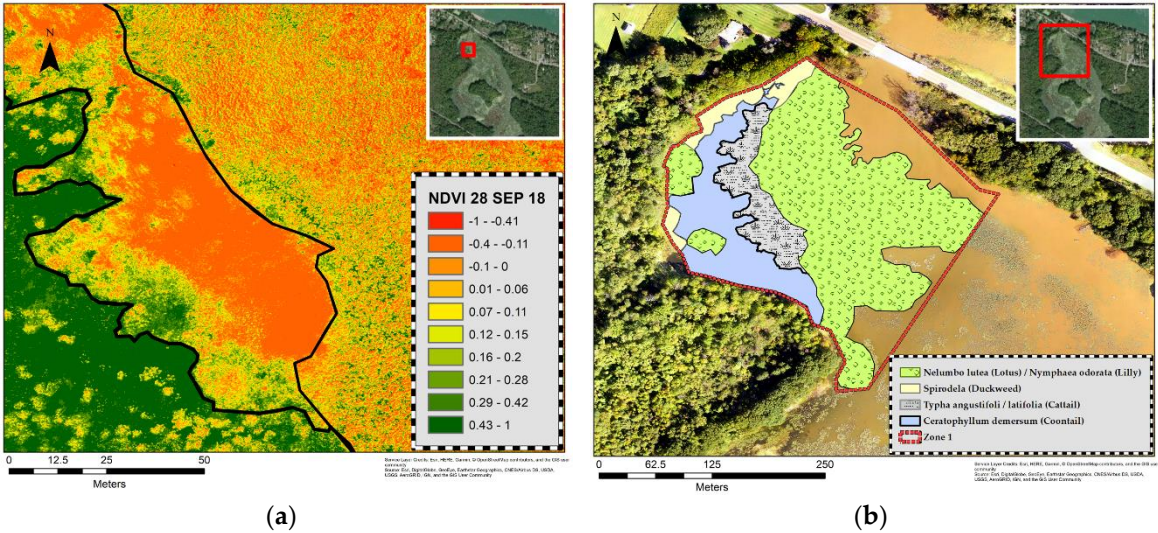287 species polygons (Figure 7b).

(**a**)   (**b**)

288 **Figure 7.** (**a**) Spectral and spatial differences between dominant species in a subsection of Zone 1; (**b**)
289 Manual classifications resulting in dominant species polygons in Zone 1.

290 The quantified areas of each dominant species type compared across scenes revealed changes
291 in vegetation coverage over time (Table 7). Ceratophyllum, a submergent vegetation species, was
292 detected on September 28th, but was completely undetectable on October 25th. This may be due to
293 differences in sun angle and brightness between both dates that resulted in greater light penetration
294 and greater reflection of Ceratophyllum from beneath the water surface, or due to the late season as
295 Ceratophyllum are typically dormant by November and would have been harder to detect as they
296 sink when dormant [53, 54].

297 **Table 7.** Vegetation extent changes over time from September to October.

298

September 28th		
Type	**Area (m^2)**	**% (Zone 1)**
Spirodela	2,635	5
Ceratophyllum	9,984	18
Typha	5,129	9
Nelumbo Lutea	29,650	53
Open Water	9,046	16
Zone 1 Total	56,444	

October 25th		
Type	**Area (m^2)**	**% (Zone 1)**
Spirodela	4,185	7
Ceratophyllum	0	0
Typha	1,667	3
Nelumbo Lutea	27,430	49
Open Water	23,161	41
Zone 1 Total	56,444	

299

300   The polygons of dominant plant species was also used to satisfy the requirements of the
301 NERRS classification system. The polygons were numbered (Figure 8) and a table of habitat
302 classifications was produced (Table 8). To be useful to NERRS wetland managers, the NERRS
303 classification must be at least to the subclass level. The RGN and RGB orthomosaics were of high
304 enough quality to satisfy the NERRS classification schemes not only to the subclass level, but
305 dominant species type could also be appended (Table 8). Similar maps could easily be used to
306 satisfy periodic surveys of habitat changes over time for wetland managers at a higher temporal
307 resolution than is currently available. The dominant species of these polygons were validated by
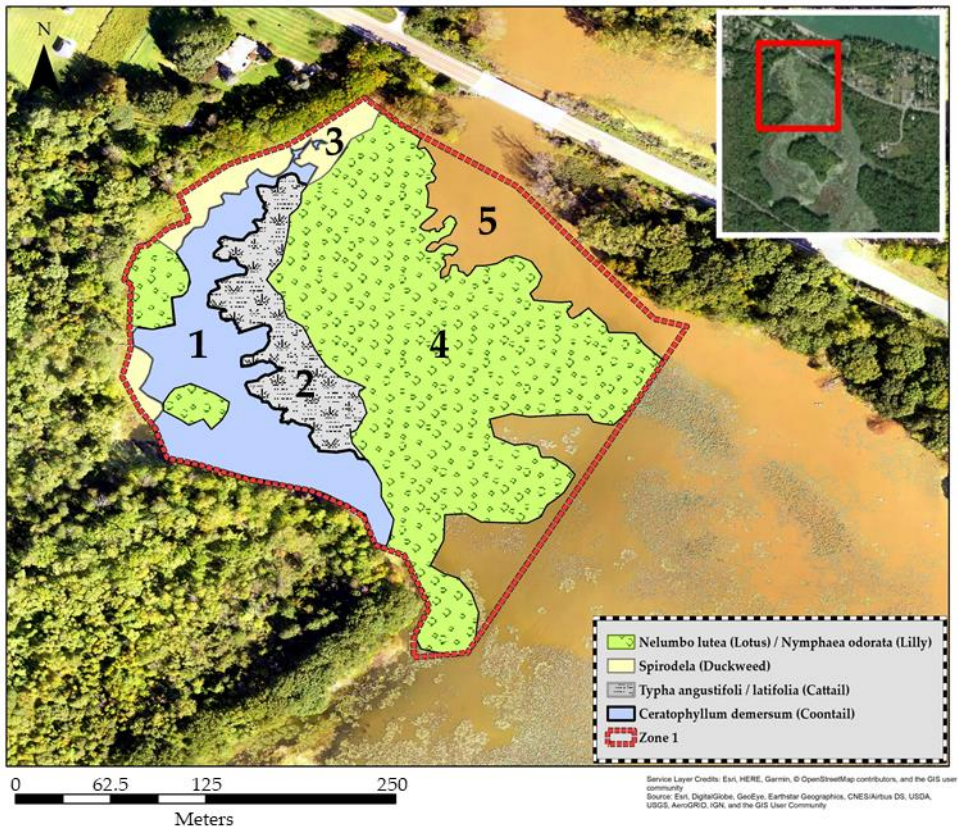308 volunteers and ecologists at OWC by boat doing concurrent studies and routine vegetation
309 monitoring.

310   **Figure 8.** NERRS Classification polygons.

311   **Table 8.** Vegetation extent changes over time from September to October.

Polygon	System	Subsystem	Class	Subclass	NERRS Code	Dominant Species
Polygon 1	Estuarine	Subtidal Fresh	Aquatic Bed	Floating Vascular	2400	Ceratophyllum demersum
Polygon 2	Estuarine	Subtidal Fresh	Emergent Wetland	Persistent	2400	Typha angustifoli / latifolia
Polygon 3	Estuarine	Subtidal Fresh	Emergent Wetland	Floating Vascular	2400	Spirodela polyrhiza
Polygon 4	Estuarine	Subtidal Fresh	Emergent Wetland	Rooted Vascular	2400	Nelumbo lutea
Polygon 5	Estuarine	Subtidal Fresh	Emergent Wetland	Unconsolidated Bottom	5100	None

312

313   *3.6 Satellite & Aerial Platform Comparison*

314   The Survey 3W camera provided a higher resolution product than available satellite or aerial
315   imagery (Figure 9). The water-land boundary was much more easily distinguished and the sUAS
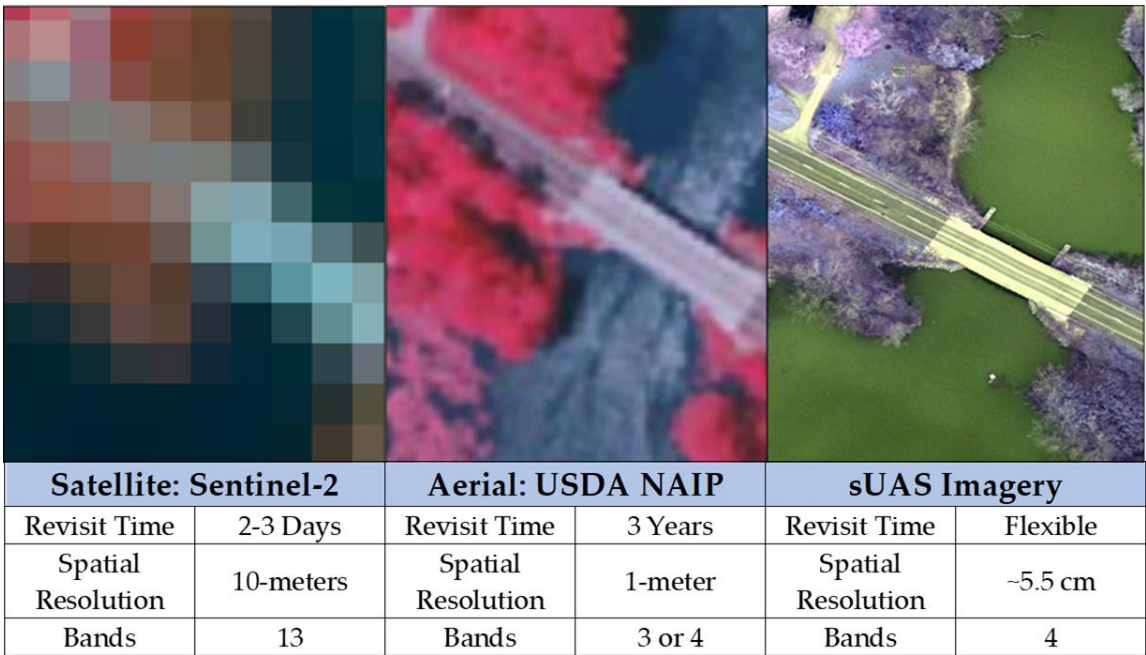316   proved to be a more flexible solution only limited by weather and batteries.

Satellite: Sentinel-2		Aerial: USDA NAIP		sUAS Imagery	
Revisit Time	2-3 Days	Revisit Time	3 Years	Revisit Time	Flexible
Spatial Resolution	10-meters	Spatial Resolution	1-meter	Spatial Resolution	~5.5 cm
Bands	13	Bands	3 or 4	Bands	4

317   **Figure 9.** Survey 3W comparison to Sentinel-2 and NAIP imagery.

318   The higher spatial resolution of the Survey 3W means a reduction in pixel mixing compared
319   to satellite and aerial imagery. Especially in satellite imagery, pixel mixing means an inability to
320   distinguish finer features in a scene and an averaging of brightness values across a single pixel
321   [6]. The Survey 3W produced much more comprehensive distinctions between not only the
322   water-land boundaries, but water-vegetation boundaries when vegetation canopy was larger
323   than 25 cm^2 and resulted in much more accurate extent measurements for areas of interest.

324   **4. Discussion**

325   The methods used in this study for planning and conducting flights would be easily
326   implemented at other wetland areas. The main challenges were planning flights around visitors and
327   finding suitable takeoff sites. Flights in this study were limited to the morning hours when foot traffic
328   was low. There were also potential takeoff sites in the southern part of the estuary, but they were
329   difficult to get to and during most of the year there was dense canopy making takeoff options limited.
330   Weather conditions, FAA Part 107 regulations, and non-interference with wildlife are considerations
331   that must be addressed by the pilot-in-command before each flight. Bi-directional reflectance and
332   variable light conditions have also been recognized in previous studies as challenges to sUAS flights
333   in previous studies and were also considerations at OWC [21].

334　　　　Sun-glint and saturation were the main spectral factors that affected the orthomosaic process.
335　　Sun-glint is a result of the bi-directional reflected light off of water surfaces at an angle such that the
336　　reflected light is pointed directly at the Survey 3W sensor [55]. All flights were conducted at about
337　　the same time of day, but the angle of the flight legs was changed for some flights as an attempt to
338　　limit sun-glint. Most flights had enough images with sufficient overlap that masking out the sun glint
339　　was not a problem regardless of flight directions, but previous studies suggest the camera be
340　　positioned 40° from nadir vertically and 135° horizontally from the sun to minimize sun-glint [56].
341　　The flexibility and repeatability of the sUAS allows for more data to be collected quickly and easily
342　　if sun-glint or saturation is too pronounced on a single flight.
343　　　　One great advantage of sUAS flights is the ability to collect data on cloudy days. The sUAS was
344　　able to fly on cloudy days and collect relevant data, especially when limited to vegetation or water
345　　extent with less consideration for density and health measurements. However, with this advantage
346　　comes the considerations and challenges with flying under cloud cover. For instance, variable cloud
347　　reflections on water proved difficult for the orthomosaic software. A flight on October 30th was flown
348　　under variable cloud cover shortly before the barrier beach was scheduled to be breached artificially,
349　　and although vegetation coverage was preserved, variable cloud cover could be seen clearly in the
350　　orthomosaics of both the RGN and RGB scenes and the brighter areas when the sun was revealed
351　　resulted in false high NDVI pixels. NDWI values for this day also resulted in inaccurate pixel
352　　classifications. In addition, the intermittent cloud cover resulted in a "flashlight" effect where part of
353　　the scene was much brighter than the surrounding flights.
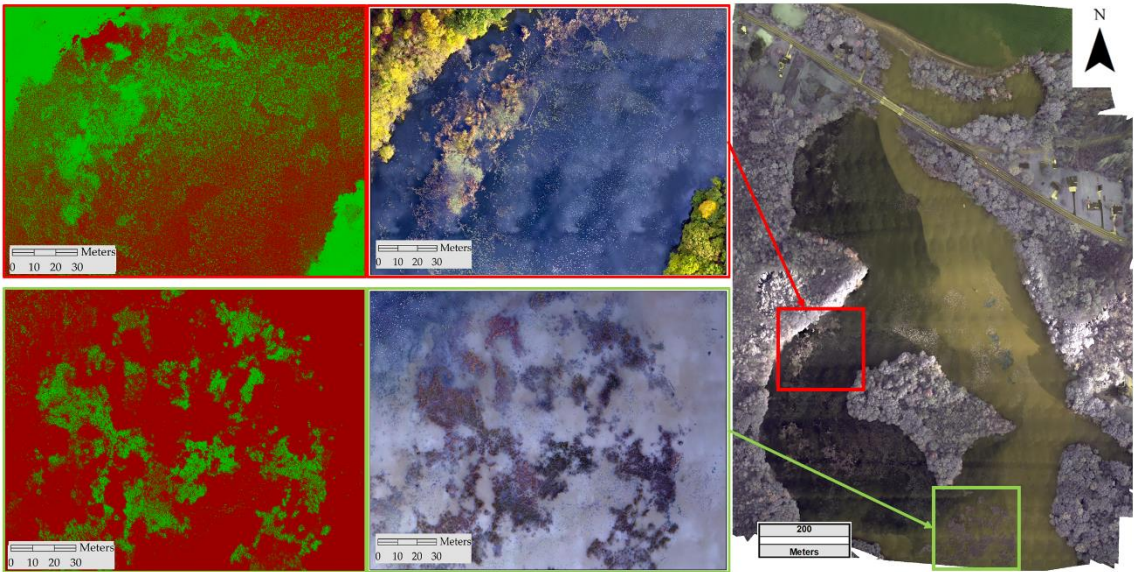
Figure 10. Flight on October 30th, 2018 under variable cloud cover displaying some orthomosaic
anomalies to include repeating cloud patterns and a flashlight effect when the sun was exposed that
created false vegetation detection in the top (red) images.

357　　　　The horizontal and vertical accuracy of the orthomosaics in this study could be improved
358　　in future studies. OWC is a homogeneously textured area resulting in a lack of tie points in
359　　forested areas. The density of the forested canopy resulted in a lack of places to put GCPs. One
360　　study suggests placing a GCP every 100 meters in any direction [57], while another suggests a
361　　GCP for every 200 m² [58] to prevent distortions. Increasing the positional accuracy of the
362　　orthomosaics would allow for volumetric calculations to be done with point cloud software with
363　　volumetric change calculation functions, especially if the GCPs were placed strategically around
364　　the submerged parts of the basin on terrestrial surfaces. OWC could install permanent or semi-
365　　permanent indicators on stable surfaces to use in continual surveys, if the GCPs were large
366　　enough to be seen clearly from the sensors.

367 **5. Conclusions**

368 SUAS offer a relatively inexpensive, accurate, and versatile method for monitoring wetland
369 systems. With the Survey 3W or a similar sensor, NDWI can detect the extent of open water and
370 inundation while NDVI can assess vegetation extent. In a managed reserve or park, routine ground
371 validation can be done with no extra effort on the part of staff and volunteers, and the addition of
372 high-resolution remote sensing data can vastly increase the understanding of local hydrologic
373 processes and vegetation habitat changes in response to these changes. The data presented is
374 sufficient to satisfy the requirements of the NERRS classification system used by the NOAA Office of
375 Coastal Management and other organizations for use in habitat monitoring over time. Classifying
376 habitat ranges over time, in combination with water level data, gives wetland managers a real time
377 idea of how wetland habitats are responding to inundation changes. The versatility of the sUAS
378 platform means inundation changes and subsequent vegetation responses can be monitored as
379 needed.

380 The cost of the sUAS platform is much more attainable to wetland managers than fixed-wing
381 manned aircraft as the entire system costs about $1,500, in addition to calibration targets ranging
382 from $300-$2,000. The same software used for this project could also be used for aerial and satellite
383 imagery, but many additional options are becoming available with the proliferation of sUAS and
384 miniaturized remote sensing technology. The sUAS method described here, when compared to
385 Sentinel-2 and NAIP data, is higher resolution and offers more flexibility and control in its
386 application.

387 SUAS applications offer a way to map wetland changes and monitor how these changes affect
388 the habitat of plant and animal life over time. In addition, this approach could be used in many
389 situations where water inundation changes and the subsequent effect on vegetation must be
390 monitored. Examples include environmental spills or disasters, flood mitigation or monitoring, or
391 habitat restorations to name a few. This method allows users to collect data in their areas of interest
392 whenever they need it instead of requiring data from other remote sensing platforms that may or
393 may not be available.

394

409 **References**

410 1. Wetzel, R.G., *Wetlands as metabolic gates.* Journal of Great Lakes Research, 1992. **18**(4): p. 529-532.

411 2. Herdendorf, C., D.M. Klarer, and R.C. Herdendorf, *The Ecology of Old Woman Creek, Ohio: An Esturine*
412   *and Watershed Profile*. 2004: Ohio Department of Natural Resources.

413 3. Woodward, R.T. and Y.-S. Wui, *The economic value of wetland services: a meta-analysis.* Ecological
414   economics, 2001. **37**(2): p. 257-270.

415   4.   Mitsch, W.J., B. Bernal, and M.E. Hernandez, *Ecosystem services of wetlands.* International Journal of
416   Biodiversity Science, Ecosystem Services & Management, 2015. **11**(1): p. 1-4.
417   5.   ESA. *Sentinel Online*. [Website] 2017 2017 4 December 2017]; Available from:
418   https://sentinel.esa.int/web/sentinel/missions/sentinel-2/data-products.
419   6.   Frazier, P.S. and K.J. Page, *Water body detection and delineation with Landsat TM data.* Photogrammetric
420   engineering and remote sensing, 2000. **66**(12): p. 1461-1468.
421   7.   Knoth, C., et al., *Unmanned aerial vehicles as innovative remote sensing platforms for high-resolution infrared*
422   *imagery to support restoration monitoring in cut-over bogs.* Applied Vegetation Science, 2013. **16**(3): p. 509-
423   517.
424   8.   McCarthy, M.J., et al., *Effects of hydrological flow regime on sediment-water interface and water column*
425   *nitrogen dynamics in a Great Lakes coastal wetland (Old Woman Creek, Lake Erie).* Journal of Great Lakes
426   Research, 2007. **33**(1): p. 219-231.
427   9.   Tomaszek, J.A., W.S. Gardner, and T.H. Johengen, *Denitrification in sediments of a Lake Erie coastal wetland*
428   *(Old Woman Creek, Huron, Ohio, USA).* Journal of Great Lakes Research, 1997. **23**(4): p. 403-415.
429   10.   Albert, D.A., et al., *Hydrogeomorphic classification for Great Lakes coastal wetlands.* Journal of Great Lakes
430   Research, 2005. **31**: p. 129-146.
431   11.   Herdendorf, C.E., *Great lakes estuaries.* Estuaries and Coasts, 1990. **13**(4): p. 493-503.
432   12.   Mouw, C.B., et al., *Aquatic color radiometry remote sensing of coastal and inland waters: Challenges and*
433   *recommendations for future satellite missions.* Remote Sensing of Environment, 2015. **160**: p. 15-30.
434   13.   Hardin, P.J. and T.J. Hardin, *Small-Scale Remotely Piloted Vehicles in Environmental Research.* Geography
435   Compass, 2010. **4**(9): p. 1297-1311.
436   14.   Watts, A.C., V.G. Ambrosia, and E.A. Hinkley, *Unmanned aircraft systems in remote sensing and scientific*
437   *research: Classification and considerations of use.* Remote Sensing, 2012. **4**(6): p. 1671-1692.
438   15.   Hinckley, T.K. and J.W. Walker, *Obtaining and Using Low-Altitude/Large Scale Imagery.* Photogrammetric
439   Engineering and Remote Sensing, 1993. **59**: p. 310-310.
440   16.   Zeng, C., et al., *Fusion of Multispectral Imagery and Spectrometer Data in UAV Remote Sensing.* Remote
441   Sensing, 2017. **9**(7): p. 696.
442   17.   Carrivick, J.L., et al., *Developments in budget remote sensing for the geosciences.* Geology Today, 2013. **29**(4):
443   p. 138-143.
444   18.   Rango, A., et al., *Using unmanned aerial vehicles for rangelands: current applications and future potentials.*
445   Environmental Practice, 2006. **8**(3): p. 159-168.
446   19.   Vivoni, E.R., et al., *Ecohydrology with unmanned aerial vehicles.* Ecosphere, 2014. **5**(10): p. art130.
447   20.   Papakonstantinou, A., K. Topouzelis, and G. Pavlogeorgatos, *Coastline zones identification and 3D coastal*
448   *mapping using UAV spatial data.* ISPRS International Journal of Geo-Information, 2016. **5**(6): p. 75.
449   21.   Rasmussen, J., et al., *Are vegetation indices derived from consumer-grade cameras mounted on UAVs*
450   *sufficiently reliable for assessing experimental plots?* European Journal of Agronomy, 2016. **74**(Supplement
451   C): p. 75-92.
452   22.   Dehm, D., *A Small Unmanned Aerial System (sUAS) Based Method for Monitoring Wetland Inundation &*
453   *Vegetation*, in *Department of Environmental Sciences*. 2019, University of Toledo: Toledo, OH. p. 120.
454   23.   Ouyang, Z., et al., *Evaluating the sensitivity of wetlands to climate change with remote sensing techniques.*
455   Hydrological Processes, 2014. **28**(4): p. 1703-1712.
456   24.   DJI, *Phantom 4 Pro*. 2018, Dà-Jiāng Innovations
457   25.   Campbell, J.B. and R.H. Wynne, *Introduction to remote sensing*. 2011: Guilford Press.

458 26. FAA. *Part 107 - Small Unmanned Aircraft Systems*. Title 14: Aeronautics & Space 2018 January 9, 2018
459 [cited 2018 January 11, 2018]; Available from: https://www.ecfr.gov/cgi-bin/text-
460 idx?SID=c0d353fab27e306b532c17cd290b59e8&mc=true&node=pt14.2.107&rgn=div5.

461 27. Gini, R., et al., *UAV photogrammetry: Block triangulation comparisons.* Int. Arch. Photogram. Remote Sens.
462 Spat. Inf. Sci, 2013. **1**: p. W2.

463 28. MAPIR. *Survey 3W Camera - Red+Green+NIR (RGN, NDVI)*. 2018 [cited 2018; Available from:
464 https://www.mapir.camera/products/survey3w-camera-red-green-nir-rgn-ndvi.

465 29. NGS. *NAVD88 - IGLD85 Height Conversion*. [Web Page] 2017 May 16, 2017 November 2018]; Available
466 from: https://www.ngs.noaa.gov/TOOLS/IGLD85/igld85.shtml.

467 30. Barrand, N.E., et al., *Optimizing photogrammetric DEMs for glacier volume change assessment using laser-
468 scanning derived ground-control points.* Journal of Glaciology, 2009. **55**(189): p. 106-116.

469 31. Becker, R.H., K.A. Zmijewski, and T. Crail, *Seeing the forest for the invasives: mapping buckthorn in the Oak
470 Openings.* Biological Invasions, 2013. **15**(2): p. 315-326.

471 32. Clark, B., J. Suomalainen, and P. Pellikka, *The selection of appropriate spectrally bright pseudo-invariant
472 ground targets for use in empirical line calibration of SPOT satellite imagery.* ISPRS journal of
473 photogrammetry and remote sensing, 2011. **66**(4): p. 429-445.

474 33. Moore, T.S., et al., *Bio-optical Properties of Cyanobacteria Blooms in Western Lake Erie.* Frontiers in Marine
475 Science, 2017. **4**: p. 300.

476 34. Agisoft, L., *Agisoft Photoscan Professional (Version 1.4.2) (Software).* Professional Edition, 2018.

477 35. Westoby, M., et al., *'Structure-from-Motion'photogrammetry: A low-cost, effective tool for geoscience
478 applications.* Geomorphology, 2012. **179**: p. 300-314.

479 36. Henriques, M.J., et al., *Assessing the Quality of an UAV-based Orthomosaic and Surface Model of a Breakwater.*
480 2014.

481 37. NUPO. *Agisoft PhotoScan Workflow*. [PDF] 2017 March 2017 [cited 2018 June 1st]; USGS Agisoft
482 Photoscan workflow for UAS]. Available from:
483 https://uas.usgs.gov/nupo/pdf/USGSAgisoftPhotoScanWorkflow.pdf.

484 38. Granshaw, S.I., *Photogrammetric Terminology: Third Edition.* The Photogrammetric Record, 2016. **31**(154):
485 p. 210-252.

486 39. McLauchlan, P.F. and A. Jaenicke, *Image mosaicing using sequential bundle adjustment.* Image and Vision
487 Computing, 2002. **20**(9): p. 751-759.

488 40. James¹, D.W., et al., *Point cloud data from Photogrammetry techniques to generate 3D Geometry.* 2015.

489 41. Smith, G.M. and E.J. Milton, *The use of the empirical line method to calibrate remotely sensed data to reflectance.*
490 International Journal of remote sensing, 1999. **20**(13): p. 2653-2662.

491 42. Farrand, W.H., R.B. Singer, and E. Merényi, *Retrieval of apparent surface reflectance from AVIRIS data: A
492 comparison of empirical line, radiative transfer, and spectral mixture methods.* Remote Sensing of
493 Environment, 1994. **47**(3): p. 311-321.

494 43. Rouse Jr, J.W., et al., *Monitoring vegetation systems in the Great Plains with ERTS.* 1974.

495 44. USGS. *NDVI, The Foundation for Remote Sensing Phenology*. Vegetation Indices [Webpage] 2015 1/12/2015
496 [cited 2018 1/25/2018]; Available from: https://phenology.cr.usgs.gov/ndvi_foundation.php.

497 45. Kutcher, T., *Habitat and land cover classification scheme for the National Estuarine Research Reserve System.*
498 The National Estuarine Research Reserve System (NERRS), 2008.

499 46. McFeeters, S.K., *The use of the Normalized Difference Water Index (NDWI) in the delineation of open water
500 features.* International journal of remote sensing, 1996. **17**(7): p. 1425-1432.

501   47.   USGS, *USGS 04199155 Old Woman Creek at Berlin Rd near Huron, OH*. 2018, U.S. Geological Survey.

502   48.   Acharya, T.D., A. Subedi, and D.H. Lee, *Evaluation of Water Indices for Surface Water Extraction in a*
503   *Landsat 8 Scene of Nepal.* Sensors (Basel, Switzerland), 2018. **18**(8): p. 2580.

504   49.   Rokni, K., et al., *Water Feature Extraction and Change Detection Using Multitemporal Landsat Imagery.*
505   Remote Sensing, 2014. **6**(5): p. 4173-4189.

506   50.   Service, N.N.O., *Tides & Currents*. 2019, Center for Operational Oceanographic Products and Services

507   51.   Verhoeven, G., *It's all about the format–unleashing the power of RAW aerial photography*. International
508   Journal of Remote Sensing, 2010. **31**(8): p. 2009-2042.

509   52.   Huete, A.R., H. Liu, and W.J. van Leeuwen. *The use of vegetation indices in forested regions: issues of linearity*
510   *and saturation*. in *Geoscience and Remote Sensing, 1997. IGARSS'97. Remote Sensing-A Scientific Vision for*
511   *Sustainable Development., 1997 IEEE International*. 1997. IEEE.

512   53.   Best, E.P.H. and J.T. Meulemans, *Photosynthesis in relation to growth and dormancy in Ceratophyllum*
513   *demersum.* Aquatic Botany, 1979. **6**: p. 53-65.

514   54.   Runkel, S. and D. Roosa, *Wildflowers and Other Plants of Iowa Wetlands*. 1999.

515   55.   Kay, S., J. Hedley, and S. Lavender, *Sun glint correction of high and low spatial resolution images of aquatic*
516   *scenes: a review of methods for visible and near-infrared wavelengths.* Remote sensing, 2009. **1**(4): p. 697-730.

517   56.   Mobley, C.D., *Estimation of the remote-sensing reflectance from above-surface measurements.* Applied optics,
518   1999. **38**(36): p. 7442-7455.

519   57.   Tonkin, T. and N. Midgley, *Ground-control networks for image based surface reconstruction: An investigation*
520   *of optimum survey designs using UAV derived imagery and structure-from-motion photogrammetry.* Remote
521   Sensing, 2016. **8**(9): p. 786.

522   58.   Oniga, V.-E., A.-I. Breaban, and F. Statescu. *Determining the optimum number of ground control points for*
523   *obtaining high precision results based on UAS images*. in *Multidisciplinary Digital Publishing Institute*
524   *Proceedings*. 2018.